DOI: 10.1002/ ((please add manuscript number))
Article type: Full Paper

P3HT Molecular Weight Determines the Performance of P3HT:O-IDTBR Solar Cells

Jafar I. Khan[†1], Raja S. Ashraf[†1,2], Maha A. Alamoudi[1], Mohammed N. Nabi[1], Hamza N. Mohammed[3], Andrew Wadsworth[4], Yuliar Firdaus[1], Weimin Zhang[1], Thomas D. Anthopoulos[1], Iain McCulloch[1], Frédéric Laquai[1]**

[1]Dr. J. I. Khan, Dr. R. S. Ashraf, M. A. Alamoudi, M. N. Nabi, Dr. Y. Firdaus, Dr. W. Zhang, Prof. T. D. Anthopoulos, Prof. I. McCulloch, Prof. F. Laquai.

King Abdullah University of Science and Technology (KAUST), KAUST Solar Center (KSC), Physical Sciences and Engineering Division (PSE), Thuwal 23955-6900, Kingdom of Saudi Arabia

[2]Dr. R.S. Ashraf

Department of Chemistry, Government College University Lahore, 54000, Lahore, Pakistan

[3]Hamza N. Mohammed

KAUST Schools, Thuwal 23955-6900, Kingdom of Saudi Arabia

[4]A. Wadsworth

Department of Chemistry and Centre for Plastic Electronics, Imperial College London, London, SW7 2AZ, UK Imperial College, London, UK

E-mail: jafar.khan@kaust.edu.sa; frederic.laquai@kaust.edu.sa

Keywords: non-fullerene acceptors, transient absorption, molecular weight, P3HT, O-IDTBR

Abstract

Large-scale production of organic solar modules requires low-cost and reliable materials with reproducible batch-to-batch properties. In case of polymers, their (photo)physical properties depend strongly on the polymers' molecular weight. Here, we study the impact of the molecular weight of the donor polymer poly(3-hexylthiophene) (P3HT) on the photophysics in blends with a recently-developed rhodanine-endcapped indacenodithiophene non-fullerene acceptor (IDTBR), a bulk heterojunction system that can potentially fulfill the aforementioned criteria for large-scale production. We find that the power conversion efficiency (PCE) increases when the weight-average molecular weight (MW) is increased from 17kDa (PCE: 4.0%) to 34 kDa (PCE: 6.6%), while a further increase in MW leads to a reduced PCE of 4.4%. We demonstrate that the charge generation efficiency, as estimated from time-delayed collection field (TDCF) experiments, varies with the P3HT molecular weight and is the reason for the differences in photocurrent and device performance. Our findings provide insight into the fundamental photophysical reasons of the molecular weight dependence of the power conversion efficiency, which has to be taken into account when using polymer-based non-fullerene acceptor blends in solar cell devices and modules.

Introduction

Organic photovoltaic (OPV) materials offer unique advantages such as low cost, synthetic variability, mechanical flexibility, transparency, lightweight, and the possibility of large-area processing by printing and other coating techniques.[1,2] Recent progress in realizing higher efficiencies in bulk heterojunction (BHJ) solar cells, comprised of interpenetrating organic donor-acceptor materials, has been driven by the development of new donor materials combined with novel non-fullerene acceptor (NFA) molecules.[3-11] NFAs, compared to fullerene derivatives, possess enhanced light absorption, band gap/energy level tunability, high charge carrier mobility, and promising photo-stability, all prerequisites for photovoltaic applications.[12] Recently, power conversion efficiencies (PCE) have approached the 15% mark, leaving the top performing fullerene-based devices behind.[3,13-16] However, when it comes to commercializing OPV, many of the donor (co)polymers developed in the past two decades have limitations due to the complexity of the required chemistry and the associated costs. Hence, the wide bandgap homopolymer regioregular poly(3-hexylthiophene) (P3HT) is still amongst the most promising and widely used polymers, when it comes to large-area printing of commercial OPV modules.[17] Consequently, P3HT in combination with fullerene derivatives has been studied intensively; however, its efficiency with fullerenes remained below 5%.[18,19] Combining P3HT with the nonfullerene acceptor O-IDTBR, improved efficiencies up to 6.3%, as has recently been demonstrated.[20,21]

The impact of the polymer's weight average molecular weight (MW) on PCE has been investigated for several polymer:fullerene systems, but contrasting trends have been observed. For instance, in the case of PTB-7, it was reported that the PCE increases with MW of the polymer primarily due to an increase in the short circuit current.[22] Similarly, the molecular weight influences the performance of P3HT-based devices such as P3HT:PCBM systems.[23,24] In this particular case, the optimum device performance was found for an

intermediate MW range around 20 kDa. It was suggested that intermediate MWs yield 'favorable morphologies' in the complex interplay of kinetics and thermodynamics during film formation, while this is not the case for higher values of MWs which showed decreased PCE. Furthermore, the MW dependence of charge transport properties of P3HT has been reported.[25] Recently, the effect of the MW of the polymer PTB7-Th (alias PCE10) when combined with O-IDTBR as acceptor was also explored. In that study, the activation energy for carrier transport in the polymer, the carrier concentration, and recombination were identified as the parameters responsible for the change in PCE.[26] Also, the effect of the MW of the acceptor in all-polymer solar cells has been reported to influence the PCE.[27] However, it is noteworthy that until now only a handful of studies have comprehensively reported time-resolved studies of the photophysical processes in polymer:NFA systems.[28]

In this work, four P3HT batches with different molecular weights (17 kDa, 34 kDa, 64 kDa, and 111 kDa) were used. The highest PCE was achieved for the intermediate molecular weight system P3HT34K:O-IDTBR (6.6%), while the PCE gradually decreased for higher molecular weights such as P3HT111K (4.4%) and for lower molecular weight P3HT17K (4.0%). Here, we address the observed differences in short circuit current density (J_{SC}) by time-resolved spectroscopy, more precisely transient absorption (TA), time-resolved photoluminescence (TR-PL), and time-delayed collection field (TDCF) experiments. TDCF measurements were used to determine the charge generation efficiency, which is identified as the factor determining the difference in short circuit current densities. We found that the trend in J_{SC} determines the trend in PCEs when varying the P3HT molecular weight. Explicitly, for the best performing system P3HT34K, the estimated charge generation efficiency is 82% compared to 52% and 49% for P3HT17K and P3HT111K, respectively. TDCF measurements further reveal weakly field-dependent charge generation in all systems in agreement with the moderate device fill factors. Finally, the J-V characteristics of all systems were successfully

reconstructed using Setfos 4.4, a commercial device simulator (FLUXiM AG) based on drift-diffusion equations, using the photophysical parameters obtained from our spectroscopic experiments.

Results and discussion

Steady-state characterization

The chemical structures of P3HT and O-IDTBR are presented in Figure 1a. The synthesis and device performance of O-IDTBR based blends have previously been reported.[20] The polydispersity index of the respective donor compounds are given in Table S2. Steady-state absorption measurements were carried out on the neat polymers, the O-IDTBR films, and on the corresponding blends, and the spectra are presented in Figure S1 and Figure S2, respectively. All P3HT films, independent of the MW of the polymer, exhibit similar spectral characteristics, a broad absorption band with three vibronic peaks in the range of 400-650 nm. O-IDTBR exhibits a weak absorption with two bands around 300-450 nm and a vibronic peak at 350 nm, and a stronger absorption band in the spectral range of 550-800 nm with a vibronic peak at 670 nm. The complementarity of the respective absorption spectra of P3HT and O-IDTBR leads to broad absorption spectra when both are blended (see Figure S1 and S2). The absorption of the P3HT:O-IDTBR blends is similar for all molecular weights studied here. In Figure 1b the extinction coefficient estimated from ellipsometry experiments is shown, confirming the similarity of the absorption of the blends.

Device characterization

BHJ solar cells were fabricated using an inverted device structure corresponding to ITO/*a*-ZnO/P3HT:O-IDTBR/MoO_3/Ag and a device area of 0.1 cm^2 and the devices were tested under AM1.5G solar illumination at an intensity of 100 mW/cm^2. The J-V characteristics of all P3HT:O-IDTBR devices are shown in Figure 1c. In addition, we prepared devices using

the conventional device structure (ITO/PEDOT:PSS/P3HT:O-IDTBR/DPO/Ag) for the best performing system. The data for this device is shown in Figure S3 and compared to the inverted device structure. The performance is similar to the inverted device structure with a slightly increased short circuit density (Table S1). The obtained figures-of-merit for optimized inverted devices using a donor:acceptor (D:A) blend ratio of 1:1 are presented in Table 1. Clearly, the PCE varies significantly with the P3HT molecular weight, mainly due to different Jsc, while the open circuit voltage is not altered (0.74-0.75 V). The fill factor varies from 58-65%, indicating differences in the field dependence of charge generation or extraction due to changes in the blend morphology as reported earlier by us and further discussed below.[21] Using electron microscopy imaging and studying the thermal behavior of blends, we previously proposed that an 'optimized morphology', in which phase separation is on the right (nm) length-scale and in which percolation pathways exist for efficient electron collection, is present in the polymer batch that gives optimal performance. At lower polymer MW, this optimal blend morphology is not present, and at higher polymer MW, the percolation pathways do not exist.[21] Images for high MW P3HT111K:O-IDTBR are presented in Figure S4, showing similar features as for the highest MW (94kDa) sample presented previously.[21] The external quantum efficiency (EQE) spectra of devices are presented in Figure 1d. The spectral response is in line with the absorption spectra of the blends, indicating both components contribute similarly to the photocurrent. The EQE follows the trend of the PCE, that is, the highest value is obtained for the P3HT34K device followed by P3HT64K, whilst P3HT111K and P3HT17K exhibit the lowest EQE values. The integrated current density is plotted alongside the EQE spectra. The obtained values are in line with the experimentally-observed short-circuit current densities.

Steady-state optical characterization

Ellipsometry was used to determine the optical constants *n* (refractive index, Figure S5) and *k* (extinction coefficient, Figure 1b) of all blends. Furthermore, the maximum possible short-circuit current densities as a function of the photoactive layer thickness were calculated by transfer matrix simulations. The results are shown in Figure S6 for the lowest and highest performing systems. The estimated $J_{SC,\,max}$ values are essentially the same for all four blends and are in the order of 20 mA/cm^2 for a layer thickness of 75 nm. We estimated from the calculated maximum short-circuit current density (~20 mA/cm^2) that the observed loss in short-circuit current density for P3HT111K:O-IDTBR and P3HT17K:O-IDTBR (10.1 mA/cm^2 and 9.1 mA/cm^2 respectively) is close to 50%, In contrast, the loss is only 33% for the best performing device P3HT34K:O-IDTBR.

Table 1: Figures-of-merit of optimized P3HT:O-IDTBR devices using different weight average molecular weights of P3HT. The blend ratio of the photoactive layer is 1:1. The values are averaged over 10 devices.

Photovoltaic Blend	D/A Ratio	V_{OC} [V]	J_{SC} [mA/cm^2]	FF [%]	PCE [%]
P3HT17K:O-IDTBR	1:1	0.74±0.01	9.1±0.2	60±1	4.0±0.1
P3HT34K:O-IDTBR	1:1	0.75±0.01	13.6±0.3	65±2	6.6±0.2
P3HT64K:O-IDTBR	1:1	0.75±0.01	12.1±0.3	63±1	5.7±0.1
P3HT111K:O-IDTBR	1:1	0.75±0.01	10.1±0.2	58±2	4.4±0.1

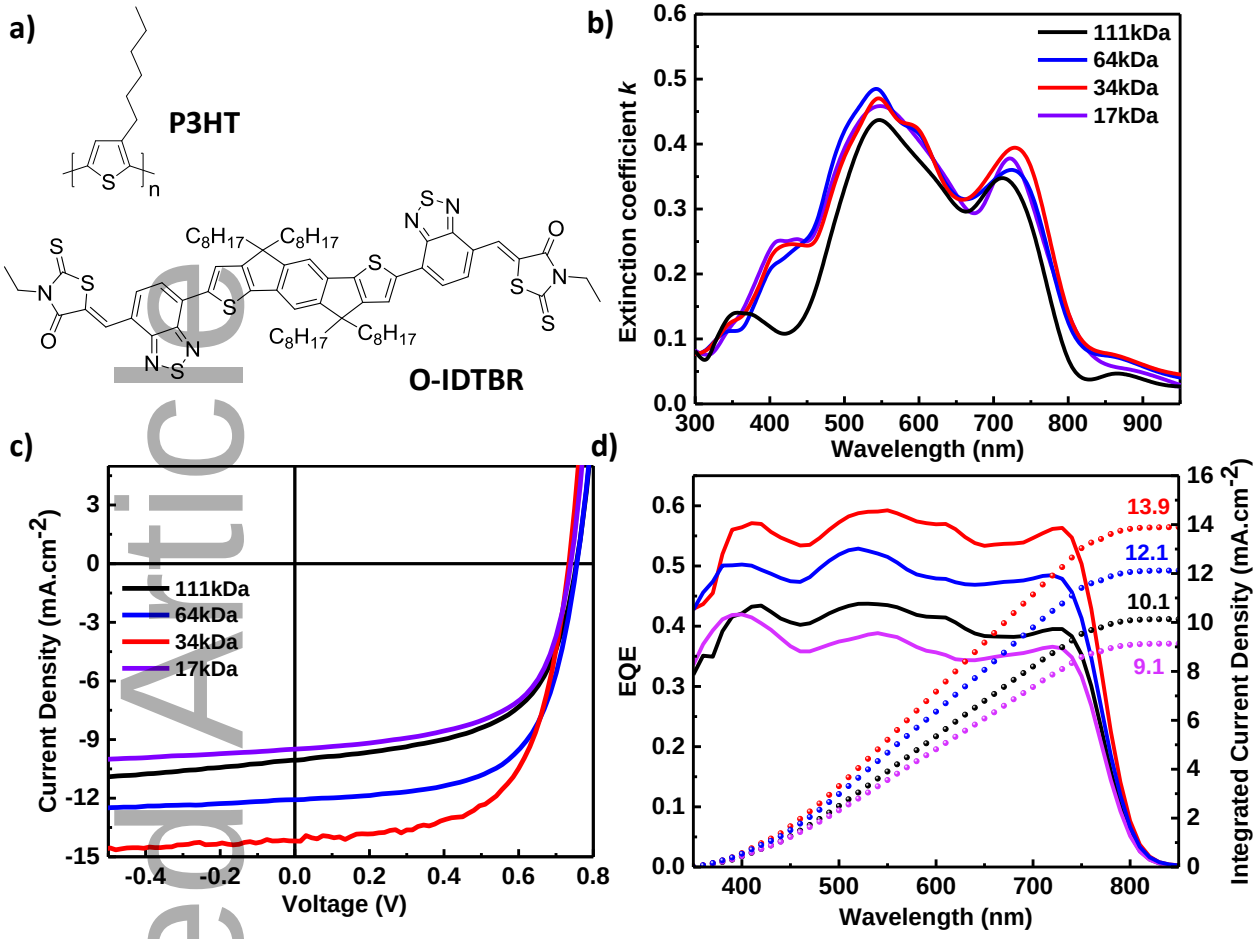

Figure 1: a) Chemical structures of the donor polymer regioregular P3HT and the nonfullerene acceptor O-IDTBR. b) Extinction coefficient *k* of the P3HT:O-IDTBR blend films with different MW (as indicated in the legend) of P3HT obtained by ellipsometry, c) J-V characteristics of P3HT:O-IDTBR devices with different P3HT MW (as indicated in the legend), and d) EQE spectra (solid lines) and corresponding integrated short circuit current density (dotted lines) of all four devices.

ps-ns exciton and charge carrier dynamics

The fluorescence dynamics of the P3HT donor polymer, the O-IDTBR nonfullerene acceptor, and the corresponding blends was investigated by TR-PL measurements. We selectively excited the blends at 550 nm and at 650 nm, which predominantly excites either the polymer or the acceptor. The transient PL spectra of pristine P3HT and O-IDTBR at different time

delays are shown in Figure S7. The pristine P3HT sample exhibits the typical broad P3HT fluorescence peaking at 730 nm.[29] All P3HT donor polymers exhibit very similar PL spectra. However, from the spectra we observe that the PL of the neat P3HT34K film decays faster compared to that of P3HT64K and P3HT111K (see Figure_S7). The PL spectrum of the O-IDTBR acceptor obtained by excitation at 650 nm peaks at 770 nm. The blends (see Figure S8 and Figure S9) exhibit slightly different spectra with two bands at 640 nm and 710 nm, respectively, when exciting at 550 nm, which predominantly excites the P3HT donor polymer. We assign these two peaks to the fluorescence of P3HT semi-crystalline regions, precisely the 0-0 and 0-1 transitions of H-aggregates in P3HT domains.[30] We hypothesize that the 0-0 transition is more prominent in the blend compared to pristine P3HT films due to reduced reabsorption. Emission from O-IDTBR is not observed, when exciting at 550 nm. In contrast, when the excitation wavelength is 650 nm (Figure S9), that is, excitation into the O-IDTBR absorption, the PL spectrum shows a P3HT emission peak at 710 nm only and an additional peak at 770 nm, which is assigned to the O-IDTBR acceptor emission.

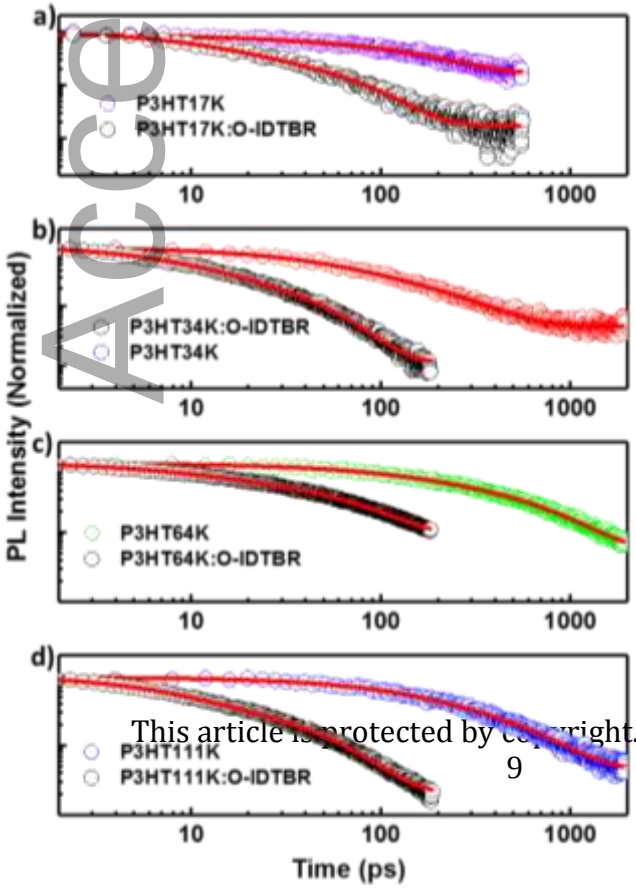

Figure 2: PL transients extracted at the peak of the P3HT emission around 725 nm following optical excitation at 550 nm. The data is plotted for the pristine P3HT donors and compared to the respective blends: a) P3HT17K:O-IDTBR, b) P3HT34K:O-IDTBR, c) P3HT64K:O-IDTBR, and d) P3HT111K:O-IDTBR. Biexponential fits to the decay profiles are indicated by solid (red) lines.

The PL decays enable us to determine the exciton quenching in the blends. The associated PL transients were tracked at the PL maxima (~725 nm) of the spectra as presented in Figure 2. In general, the blend PL exhibits faster decay compared to the pristine materials confirming the PL quenching. To analyze the exciton dynamics further, the decay kinetics were parametrized with the sum of two exponentials and the weighted-average lifetimes were calculated. The lifetime quenching was calculated by $1-(\tau_{blend}/\tau_{neat})$, where τ_{blend} and τ_{neat} are the weighted-average lifetimes of the neat film and blends, respectively. Consequently, the highest lifetime quenching efficiency is found for P3HT111K:O-IDTBR (93%), followed by 90% for P3HT64K:O-IDTBR, and 84% for P3HT34K:O-IDTBR, whilst the lowest molecular weight P3HT17K:O-IDTBR exhibits only 80% quenching. We conclude that efficient exciton quenching is obtained in all four systems and that the lowest quenching efficiency observed for P3HT17K:O-IDTBR can in part account for its lower performance. However, the exciton quenching does not entirely explain the lower short-circuit current density observed for this system.

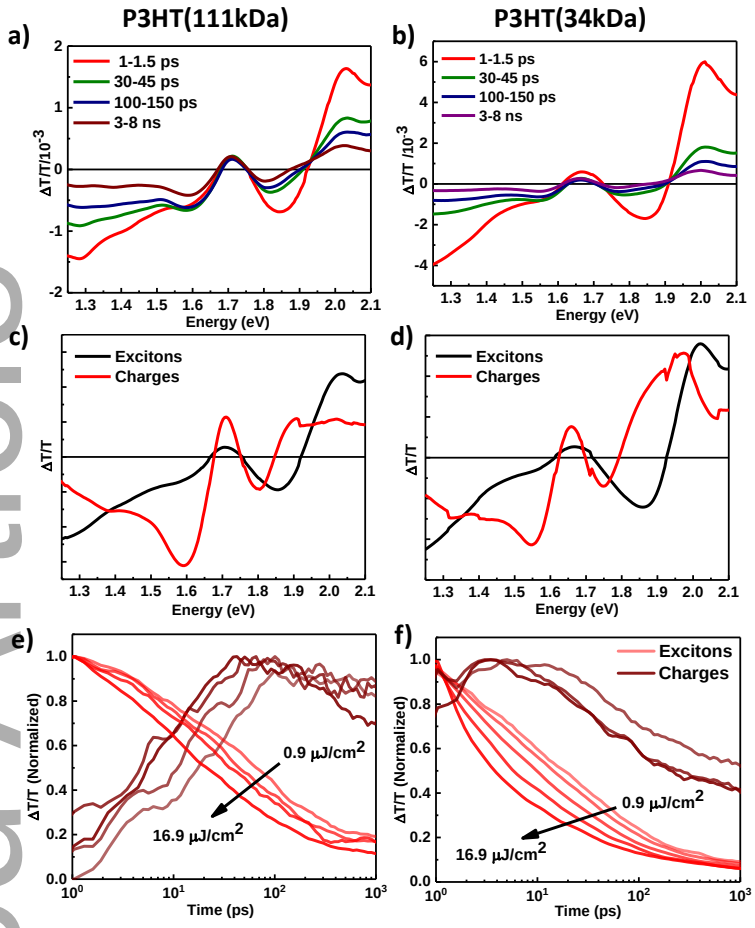

Figure 3: ps-ns TA data of the lowest (left column: 111kDa) and the highest (right column: 34kDa) performing P3HT:O-IDTBR blends after optical excitation at 532 nm: a) ps – ns TA spectra of P3HT111K:O-IDTBR; b) ps – ns TA spectra of P3HT34K:O-IDTBR; c) Component spectra obtained by MCR analysis of TA data in a); d) Component spectra obtained by MCR analysis of TA data in b); Component dynamics as extracted by MCR analysis for excitons and charge carriers at different fluences for: e) P3HT111K:O-IDTBR and f) P3HT34K:O-IDTBR.

TA experiments on the ps-ns time scale were performed following optical excitation at 532 nm to study the charge generation and recombination dynamics. The TA spectra for the highest and lowest performing systems for various pump-probe time delays can be found in

Figure 3a and 3b. The characteristic P3HT ground state bleach (GSB) is observed from 1.95 eV- 2.2 eV and the O-IDTBR GSB in the region of 1.65 eV-1.72 eV. Furthermore, two distinct regions of photoinduced absorption (PA) are observed: from 1.2 eV-1.65 eV and from 1.75 eV–1.9 eV, which we both attribute to exciton-induced absorption. Additionally, an isosbestic point is observed at 1.45 eV, which is also seen in P3HT:PCBM systems as reported earlier by Howard et al.[31] The low-energy PA region (1.2-1.65 eV) consists of contributions from two components, one, which peaks instantaneously, that is, within the instrument response time, and then decays within 30 ps. A second component with a flat PA spectrum is clearly observed after 100 ps. We assign the first component to exciton-induced absorption and the second component to charge-induced absorption. We note that the GSB of the O-IDTBR does not undergo any significant spectral changes or decay. Furthermore, any other spectral changes are negligible and similar in all four systems. We note that the charge-induced signal (ΔT/T signal amplitude at zero time) decreases in the order: P3HT34K:O-IDTBR, P3HT64K:O-IDTBR, P3HT111K:O-IDTBR, and P3HT17K:O-IDTBR in line with the short-circuit photocurrents and efficiencies of the blends. The kinetics in the PA region from 1.2-1.4 eV obtained at different fluences are plotted for all four samples in Figure S10. In all cases, the dynamics are fluence dependent and the fastest exciton decay is obtained for the P3HT34K:O-IDTBR sample in line with the time-resolved photoluminescence experiments.

In order to separate the contributions of excitons and charges, multivariate curve resolution (MCR) analysis was applied.[32] The component-associated spectra of the MCR analysis for the highest and lowest performing system are depicted in Figure 3c and 3d, respectively. The MCR analysis shows two components: singlet excitons at early delay times and charges on longer time scales. Note that the component spectra contain the spectral contributions from the donor polymer and O-IDTBR acceptor, which were not further separated here. The

component-associated dynamics obtained by MCR analysis for both systems are plotted in Figure 3e and 3f for several fluences. As mentioned, the exciton decay starts after 1 ps and the charge generation follows immediately. However, we also observe some fraction of ultrafast charge generation in both systems indicated by a 10% signal amplitude of charges at 1 ps in P3HT111K:O-IDTBR and 60% in P3HT34K:O-IDTBR. A direct comparison of the charge carrier dynamics of the P3HT111K:O-IDTBR and P3HT34K:O-IDTBR system clearly shows a delayed and diffusion-limited charge generation in the former, where the process takes about 50-60 ps, while for the latter the corresponding time scale is only 2-3 ps. This suggests that the domain size of the former system is larger, which is consistent with the findings reported earlier.[21] The fluence dependent decay of the exciton-induced absorption is attributed to exciton-exciton annihilation, as typical for TA experiments at high fluences. However, a carrier loss mechanism causing the drop in short-circuit current density is not evident from the ps-ns TA data.

ns-µs charge carrier recombination and extraction

The charge carrier recombination is further examined in the nanosecond-microsecond (ns- µs) time range. Figure S11a) and Figure S11b) shows the TA spectra of P3HT34K:O-IDTBR and P3HT111K:O-IDTBR at selected time points for a moderate fluence of 7.3 µJ/cm^2. From the spectral evolution of the PA region at 1.22-1.4 eV of the two systems, it is apparent that the low molecular weight system exhibits faster recombination than the high molecular weight one. The charge-induced signal decays entirely within 100-150 ns for P3HT34K:O-IDTBR in contrast to 300-450 ns for P3HT111K:O-IDTBR. Furthermore, a minor difference is observed in the charge carrier dynamics of the blends. Figure S11c) and S11d) show that the charge carrier dynamics is fluence independent in the first 3-4 ns for P3HT111K:O-IDTBR and P3HT17K:O-IDTBR, indicating geminate recombination occurs on this time scale. For

P3HT64K:O-IDTBR and P3HT34K:O-IDTBR blends we also observe a fluence independent decay in the first 2 ns. However, the low molecular weight blends exhibit overall a faster decay in contrast to the high molecular weight ones.

Table 2: Bimolecular recombination coefficients of all systems determined from TA and TDCF.

Photovoltaic Blend	k_{BM} (TA) cm^3s^{-1}	k_{BM} (TDCF) cm^3s^{-1}
P3HT17K:O-IDTBR	6.9×10^{-9}	9.4×10^{-11}
P3HT34K:O-IDTBR	2.5×10^{-11}	7.3×10^{-12}
P3HT64K:O-IDTBR	6.0×10^{-11}	3.5×10^{-11}
P3HT111K:O-IDTBR	2.4×10^{-10}	6.4×10^{-11}

We determined the bimolecular recombination coefficient k_{BM} from TA and TDCF measurements, respectively (see below). A comparison for all blends is shown in Table 2. The values of k_{BM} from the TA data were estimated by fitting the ns-µs TA charge carrier dynamics in the PA region to a two-pool recombination model as reported earlier for other BHJ systems.[31] In the TDCF experiment, the time delay t_{del} between the generation and collection of charge carriers was varied. The quantity of collected charge Q_{coll} as a function of t_{del} was then fitted using a model developed earlier and reported in the literature.[33,34] We note that the values obtained from TA and TDCF are within the same order for P3HT34K:O-IDTBR, P3HT64K:O-IDTBR, and P3HT111K:O-IDTBR, while it is two orders of magnitude higher for P3HT17K:O-IDTBR. The difference in the bimolecular recombination coefficient of the lowest P3HT molecular weight system is most likely caused by the relatively fast decay

of charge carriers seen from the TA experiment, indicating that fitting the dynamics overestimates the value. We have discussed the difference of recombination coefficients obtained by TA and TDCF earlier, however, typically the bimolecular recombination coefficient obtained by TDCF is larger than that obtained by TA experiments, as a consequence of an overestimation of the charge recombination and possible presence of dark (injected) charge carriers.[35] Here, both techniques yield similar values with the exception of the lowest molecular weight polymer.

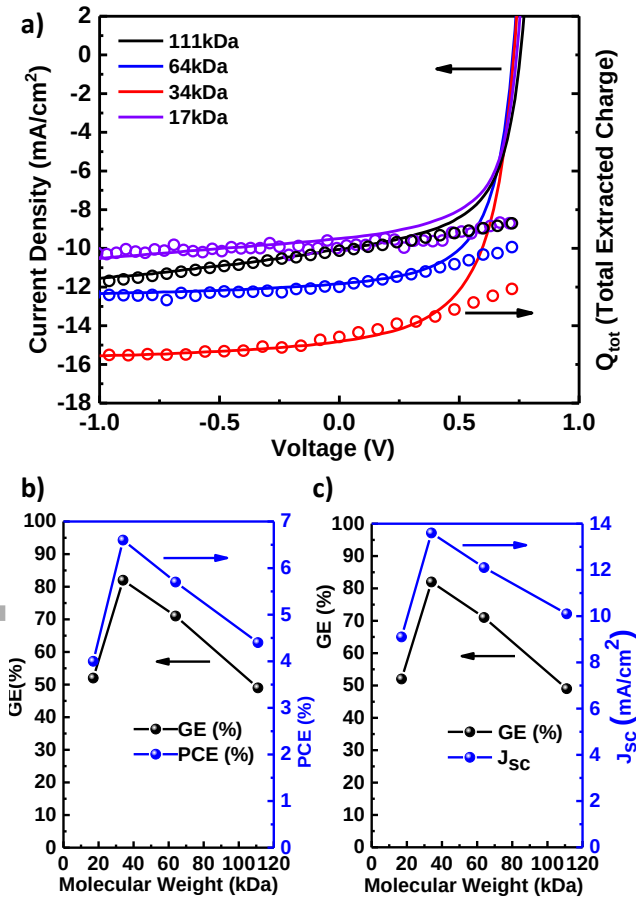

Figure 4: a) Total collected charge as a function of applied bias from TDCF measurements (dots) alongside the J-V characteristics (solid lines) for all P3HT devices for a bias range from -1V to Voc. b) Charge generation efficiency (GE) as determined from TDCF measurements as a function of the P3HT molecular weight compared to the trend of the PCE and the J_{SC} for

representative devices. A quantitative agreement with the variation in PCE is apparent from b), while c) shows a similar trend is also observed for the device short circuit current.

Time-delayed collection field measurements were also conducted to investigate a potential field dependence of charge generation. The devices were photoexcited with a nanosecond laser pulse while being kept at a constant pre-bias. The voltage of the pre-bias was then varied from -2 V to 0.75 V, ranging from negative to around open-circuit voltage. A high negative collection bias of -4 V was applied 10 ns after photoexcitation to ensure extraction of separated charge carriers prior to their recombination. In the experiment, the excitation fluence was kept low to avoid non-geminate recombination losses prior to carrier extraction. Under these conditions, the total collected charge Q_{tot} is a measure of the amount of free charges generated by photoexcitation as a function of the applied pre-bias. Figure 4a presents the data of the TDCF measurements for a pre-bias range from -2V to V_{OC}. The TDCF data (collected charge) is overlaid with the J-V characteristics of the devices (solid lines) for all four systems. The J-V curves were measured for the same device used in the TDCF measurements. Clearly, all four systems exhibit a pre-bias dependence (field dependence) of Q_{tot}, as Q_{tot} varies with the applied pre-bias, which is different from P3HT:PCBM devices reported earlier, which did not exhibit a field-dependent charge generation.[36] Surprisingly, the effect is less prominent for P3HT17K:O-IDTBR, whilst both P3HT111K:O-IDTBR and P3HT34K:O-IDTBR exhibit a stronger field dependence than P3HT64K:O-IDTBR. In all four samples, the field dependence resembles the slope of the J-V curves, implying that the fill factor is predominantly determined by the field dependence of charge generation. However, beyond the maximum power point (towards V_{oc}), non-geminate recombination losses increase as extraction slows down and the bias dependence of the J-V curves deviates from the bias dependence of Q_{tot} obtained from TDCF experiments. We note, that the field dependence of charge generation deduced from TDCF experiments has very recently been

questioned by Würfel et al., and in some cases an apparent field dependence of charge generation might be caused by fast non-geminate recombination of photogenerated and dark (injected) charge carriers.[37] At this point, we cannot entirely rule out that this is also the case for the P3HT:O-IDTBR systems studied here, but we stress that the bias dependence of the photocurrent cannot account for the performance differences that we observe.

Fluence dependent TDCF experiments were performed to determine the total number of charges collected. The data is used to calculate the initial charge carrier density N_0 for all systems (Table S3) as a function of fluence in the range from 0.05 to 5 μJ/cm^2. The calculation of the charge carrier density is given in the SI. From the comparison of the fluences used in TDCF and TA, we anticipate that the charge carrier density is overestimated for higher fluences, as the dependence on the fluence is nonlinear in both cases.

Furthermore, the loss in photocurrent was investigated by calculating the generation efficiency (GE) as detailed in the SI obtained from the TDCF data. The highest generation efficiency is obtained for P3HT34K:O-IDTBR (82%), while lower for P3HT64K:O-IDTBR (71%), P3HT17K:O-IDTBR (49%), and P3HT111K:O-IDTBR (52%), respectively. Clearly, the values are consistent with the trend of the photocurrent and photovoltaic device performance. Thus, it appears that differences in charge generation govern the device PCE. In fact, the estimated GEs are shown in Figure 4b alongside the obtained PCE values of all four devices, indicating a clear correlation between the GE and PCE. The main difference in PCE stems directly from the difference in short-circuit current density, as obvious from a plot of GE and J_{SC} presented in Figure 4c. The observed trend is similar as for the PCE. Again, this implies that the loss in short-circuit current density is due to differences in the generation efficiency associated with the different donor polymer molecular weights. In particular, this finding supports the reasons previously brought forward such as changes in morphology and

charge carrier mobility and it yields additional insight into the efficiency-limiting processes in P3HT:O-IDTBR systems.

Drift-diffusion simulation of device characteristics

The hole mobilities and electron mobilities of the respective blends were determined by SCLC measurements to be on the order of 10^{-4} $cm^2V^{-1}s^{-1}$ in all systems with little variation from system to system (see Table 3). The differences are too small to explain the differences in PCE's and photocurrents, while the trend is in line with the device performance. We used the photophysical parameters obtained by spectroscopic experiments to simulate the J-V characteristics of the devices and evaluate their relevance to describe the device physics under solar illumination. We used the commercial numerical drift-diffusion device simulation tool Setfos 4.4 (FLUXiM AG) to simulate the J-V curves as shown in Figure 5. Table 3 summarizes the input parameters and the calculated figures-of-merit of the devices. The simulation was performed using the optical constants (Figure S5), namely the refractive index (n) and extinction coefficient (k) values, obtained by ellipsometry measurements, the electron and hole mobilities measured by space-charge-limited current (SCLC) experiments, and the bimolecular recombination coefficient k_{BM} obtained by TDCF measurements. The k_{BM} values were varied in the simulation and the optimum values are given as k_{sim} in Table 3. Furthermore, the HOMO and LUMO energies reported in literature were used as input parameters.[20] Implementing the aforementioned parameters, the J-V curves were reconstructed and J_{SC}, V_{OC}, FF, and PCE were obtained. The reconstructions are in good agreement with the experimentally measured J-V curves for all systems as shown in Figure 5. Additionally, it is noteworthy that the (bimolecular) recombination coefficient obtained from TDCF measurements yields more accurate reconstructions compared to the one obtained from the fit of the charge carrier dynamics observed by TA experiments. We hypothesize, the

reason is that the initial carrier concentration of the respective measurements is significantly different, in turn affecting the obtained value of the recombination coefficient due to its carrier density dependence. However, up to now, no study has addressed this specific issue. The applicability of recombination coefficients obtained from TA, and TDCF data for the simulation of device J-V curves is subject of ongoing studies.

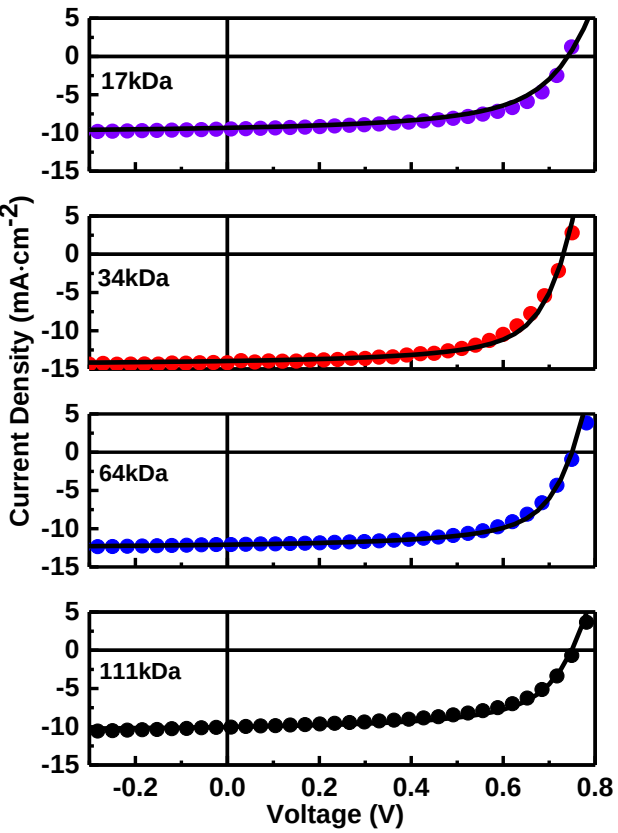

Figure 5: Current density-voltage (J-V) characteristics simulated by numerical drift-diffusion simulations using the experimentally-obtained photophysical parameters as input alongside the experimentally-measured J-V characteristics.

Table 3: Input parameters (charge carrier mobility, recombination rate) used for the simulation of *J-V* curves of P3HT:O-IDTBR solar cells as shown in Figure 5 (HOMO level:

5.0 eV, LUMO level: 3.6 eV, active layer thickness: 75 nm). Solar cell figures of merit (V_{OC}, J_{SC}, FF, and PCE) obtained from simulations are also displayed.

Blend	μ_h	μ_e	*IQE*	k_{sim}	V_{oc}	J_{sc}	FF	PCE
	$cm^2V^{-1}s^{-1}$	$cm^2V^{-1}s^{-1}$	%	cm^3/s	V	$mAcm^{-2}$	%	%
P3HT17K:O-IDTBR	1.8×10^{-4}	1.4×10^{-4}	47	9.7×10^{-11}	0.74	9.0	57	3.95
P3HT34K:O-IDTBR	3.3×10^{-4}	3.2×10^{-4}	69	6.4×10^{-11}	0.73	14.0	66	6.70
P3HT64K:O-IDTBR	3.1×10^{-4}	3.0×10^{-4}	59	7.3×10^{-11}	0.75	12.1	65	5.93
P3HT111K:O-IDTBR	2.6×10^{-4}	2.2×10^{-4}	50	9.7×10^{-11}	0.75	10.0	62	4.66

Conclusion

We have demonstrated that the donor polymer (P3HT) molecular weight plays a crucial role for the device performance in blends with O-IDTBR as non-fullerene acceptor. A weight-average molecular weight of 34 kDa was found to yield the highest PCE of 6.6%, while both lower and higher molecular weights result in a decrease in device performance. The observed differences in short circuit current density are correlated with the charge generation efficiencies, which appears to be optimal for a molecular weight of 34 kDa. In essence, the donor molecular weight governs the power conversion efficiency of P3HT:O-IDTBR devices by altering the charge generation efficiency, linked to changes in the morphology of the blends and component separation. We believe our findings have implications beyond the investigated material system and that the donor polymer's molecular weight has to be carefully considered when it comes to application of polymer:NFA systems in devices.

Experimental Section

Materials: The O-IDTBR non fullerene acceptor was synthesized as described in our previous work.[20] Moreover, the P3HT donor materials were purchased from BASF (P3HT64K), Ossila (P3HT34K), while P3HT111K and P3HT17K were synthesized in our laboratory.

OPV devices. Bulk heterojunction solar cells were fabricated with an inverted device architecture (glass/ITO/ZnO/P3HT:O-IDTBR/MoO_3/Ag). Glass substrates with pre-patterned indium tin oxide (ITO) were cleaned by sonication in detergent, deionized water, acetone and isopropanol, followed by oxygen plasma treatment. ZnO layer (10-15 nm) was deposited by spin-coating a zinc oxide nanoparticle solution (2.5 wt.% in 2-propanol)followed by annealing at 110 °C for 10 minutes. The P3HT:O-IDTBR active layers (80-100 nm) were deposited from 24 mg/ml solutions in chlorobenzene by spin-coating at 1500-2000 rpm, followed by annealing at 130 °C for 10 minutes inside the glovebox. MoO_3 (10 nm) and Ag (100 nm) layers were deposited by evaporation through a shadow mask yielding active areas of 0.1 cm^2 in each device. The *J–V* characteristics were measured using a Xenon lamp inside a glovebox using a Keithley 2400 source meter in the dark and under illumination by a simulated 100 mW cm^{-2} AM1.5G light source using Oriel Sol3A Class AAA solar simulator calibrated to 1 sun, AM1.5G, with a KG-5 silicon reference cell certified by Newport. External Quantum Efficiency (EQE) measurements were performed at zero bias by illuminating the device with monochromatic light supplied from a Xenon arc lamp in combination with a dual-grating monochromator. The number of photons incident on the sample was calculated for each wavelength by using a silicon photodiode calibrated by NIST.

UV-Vis and PL spectroscopy: Steady-state absorption measurements were conducted using a Cary 5000 UV-visible spectrometer (Agilent Technologies).

Ultrafast time-resolved measurements: Transient absorption (TA) spectroscopy was carried out using a home-built pump-probe setup. Two distinct configurations of the setup were

applied for either short delay, namely 100 fs to 8 ns experiments, or long delay, namely 1 ns to 100 μs delays, as described below.

The fundamental 800 nm output of titanium:sapphire amplifier (Coherent LEGEND DUO, 4.5 mJ, 3 kHz, 100 fs) was split into three beams (2 mJ, 1 mJ, and 1.5 mJ). The first two components were used separately to pump two optical parametric amplifiers (OPA) (Light Conversion TOPAS Prime). TOPAS 1 generates tunable pump pulses, while TOPAS 2 generates signal (1300 nm) and idler (2000 nm) only. For short delay TA measurements, TOPAS 1 was used for producing pump pulses while the probe pathway length to the sample was kept constant at approximately 5 meters between the output of the TOPAS 1 and the sample. The pump pathway length was varied between 5.12 and 2.6 m with a broadband retroreflector mounted on automated mechanical delay stage (Newport linear stage IMS600CCHA controlled by a Newport XPS motion controller), thereby generating delays between pump and probe from -400 ps to 8 ns. For measuring TA whole visible range, we used 1300 nm (signal) of TOPAS 2 focused onto a calcium fluoride crystal, thereby generating a white-light supercontinuum from 350 to 1100 nm. For the 1 ns to 100 μs delay (long delay) TA measurements, the same probe white-light supercontinuum as for the 100 fs to 8 ns delays was used. However, the excitation light (pump pulse) was provided by an actively Q-switched Nd:YVO_4 laser (INNOLAS picolo AOT) frequency-doubled to provide pulses at 532 nm. The laser was triggered by an electronic delay generator (Stanford Research Systems DG535), itself triggered by the TTL sync from the Legend DUO, allowing control of the delay between pump and probe with a jitter of roughly 100 ps.

Pump and probe beams were focused on the sample, which was kept under a dynamic vacuum of $<10^{-5}$ mbar. The transmitted fraction of the white light was guided to a custom-made prism spectrograph (Entwicklungsbüro Stresing) where a prism dispersed it onto a 512 pixel NMOS linear image sensor (HAMAMATSU S8381-512). The probe pulse repetition rate was 3 kHz,

while the excitation pulses were mechanically chopped to 1.5 kHz (100 fs to 8 ns delays) or directly generated at 1.5 kHz frequency (1 ns to 100 μs delays), while the detector array was read out at 3 kHz. Adjacent diode readings corresponding to the transmission of the sample after excitation and in the absence of an excitation pulse were used to calculate ΔT/T. Measurements were averaged over several thousand shots to obtain a good signal-to-noise ratio. The chirp induced by the transmissive optics was corrected with a home-built Matlab code by revaluating for each wavelength the delay at which pump and probe are simultaneously arriving on the sample as the time of the signal amplitude.

Time-resolved photoluminescence spectroscopy: For TR-PL experiments samples were excited with the wavelength-tunable output of an OPO (Radiantis Inspire HF-100), itself pumped by the fundamental of a Ti:sapphire fs-oscillator (Spectra Physics MaiTai eHP) at 820 nm. The repetition rate of the fs pulses was adjusted by a pulse picker (APE Pulse Select). Typical pulse energies were in the range of several nJ. The PL of the samples was collected by an optical telescope (consisting of two plano-convex lenses) and focused on the slit of a spectrograph (PI Spectra Pro SP2300) and detected with a Streak Camera (Hamamatsu C10910) system with a temporal resolution of 1.4 ps. The data was acquired in photon counting mode using the Streak Camera software (HPDTA) and exported to Origin Pro 2015 for further analysis.

Time delayed collection field (TDCF): The home-built TDCF setup uses the second harmonic (532 nm) of an actively Q-switched sub-ns Nd:YVO_4 laser (INNOLAS picolo AOT) operating at 5 kHz as excitation. To minimize the RC response time, a small device area of 1 mm^2 is used. The samples were measured under dynamic vacuum conditions to avoid any degradation. A Keysight S1160A functional generator was used to provide the pre-bias and extraction bias, while a Keysight four channel digital oscilloscope was used to measure the current response of the device.

AUTHOR INFORMATION
Corresponding Authors
email: frederic.laquai@kaust.edu.sa
jafar.khan@kaust.edu.sa

Webpage:

Ultrafast Dynamics Group: https://ufd.kaust.edu.sa

Orcid:

Jafar I. Khan: 0000-0001-6003-5641

Frédéric Laquai: 0000-0002-5887-6158

Notes
J.I.K. and R.S.A. contributed equally to the work.
The authors declare no competing financial interest.

ACKNOWLEDGMENT

The research reported in this publication was supported by the Office of Sponsored Research (OSR) under the Grant Agreement FCS/1/3321/01 and by baseline funding from the King Abdullah University of Science and Technology (KAUST). M. A. A. is grateful to Saudi Basic Industries Corporation (SABIC) for funding received towards the PhD. H.N.M. thanks the KAUST SRSI program for support. J.I.K. and R.S.A. contributed equally to the work.

Supporting Information
Supporting Information is available from the Wiley Online Library or from the author.

Received: ((will be filled in by the editorial staff))
Revised: ((will be filled in by the editorial staff))
Published online: ((will be filled in by the editorial staff))

REFERENCES

[1] N. Li, I. McCulloch, C. J. Brabec, *Energy Environ. Sci.* **2018**, *11*, 1355.

[2] P. Cheng, G. Li, X. W. Zhan, Y. Yang, *Nat. Photonics* **2018**, *12*, 131.

[3] Z. Zheng, Q. Hu, S. Q. Zhang, D. Y. Zhang, J. Q. Wang, S. K. Xie, R. Wang, Y. P. Qin, W. N. Li, L. Hong, N. N. Liang, F. Liu, Y. Zhang, Z. X. Wei, Z. Y. Tang, T. P. Russell, J. H. Hou, H. Q. Zhou, *Adv. Mater.* **2018**, *30*, 1801801.

[4] G. Y. Zhang, J. B. Zhao, P. C. Y. Chow, K. Jiang, J. Q. Zhang, Z. L. Zhu, J. Zhang, F. Huang, H. Yan, *Chem. Rev.* **2018**, *118*, 3447.

[5] Y. X. Li, L. Zhong, B. Gautam, H. J. Bin, J. D. Lin, F. P. Wu, Z. J. Zhang, Z. Q. Jiang, Z. G. Zhang, K. Gundogdu, Y. F. Li, L. S. Liao, *Energy Environ. Sci.* **2017**, *10*, 1610.

[6] Y. X. Li, J. D. Lin, X. Z. Che, Y. Qu, F. Liu, L. S. Liao, S. R. Forrest, *J. Am. Chem. Soc.* **2017**, *139*, 17114.

[7] S. Holliday, R. S. Ashraf, A. Wadsworth, D. Baran, S. A. Yousaf, C. B. Nielsen, C. H. Tan, S. D. Dimitrov, Z. R. Shang, N. Gasparini, M. Alamoudi, F. Laquai, C. J. Brabec, A. Salleo, J. R. Durrant, I. McCulloch, *Nat. Commun.* **2016**, *7*,11585.

[8] D. Baran, R. S. Ashraf, D. A. Hanifi, M. Abdelsamie, N. Gasparini, J. A. Rohr, S. Holliday, A. Wadsworth, S. Lockett, M. Neophytou, C. J. M. Emmott, J. Nelson, C. J. Brabec, A. Amassian, A. Salleo, T. Kirchartz, J. R. Durrant, I. McCulloch, *Nat. Mater.* **2017**, *16*, 363.

[9] C. Q. Yan, S. Barlow, Z. H. Wang, H. Yan, A. K. Y. Jen, S. R. Marder, X. W. Zhan, *Nat. Rev. Mater.* **2018**, *3*, 18003.

[10] Y. Xie, W. Huang, Q. Liang, J. Zhu, Z. Cong, F. Lin, S. Yi, G. Luo, T. Yang, S. Liu, Z. He, Y. Liang, X. Zhan, C. Gao, H. Wu, Y. Cao, *ACS Energy Lett.* **2019**, *4*, 8.

[11] W. Wang, B. Zhao, Z. Cong, Y. Xie, H. Wu, Q. Liang, S. Liu, F. Liu, C. Gao, H. Wu, Y. Cao, *ACS Energy Lett.* **2018**, *3*, 1499.

[12] J. Hou, O. Inganäs, R. H. Friend, F. Gao, *Nat. Mater.* **2018**, *17*, 119.

[13] S. Li, L. Ye, W. Zhao, H. Yan, B. Yang, D. Liu, W. Li, H. Ade, J. Hou, *J. Am. Chem. Soc.* **2018**, *23*, 7159.

[14] W. Zhao, S. Li, H. Yao, S. Zhang, Y. Zhang, B. Yang, J. Hou, *J. Am. Chem. Soc.* **2017**, *139*, 7148.

[15] W. Zhao, D. Qian, S. Zhang, S. Li, O. Inganäs, F. Gao, J. Hou, *Adv. Mater.* **2016**, *28*, 4734.

[16] H. Zhou, Y. Zhang, C.-K. Mai, S. D. Collins, G. C. Bazan, T.-Q. Nguyen, A. J. Heeger, *Adv. Mater.* **2015**, *27*, 1767.

[17] N. Espinosa, M. Hösel, M. Jørgensen, F. C. Krebs, *Energy Environ. Sci.* **2014**, *7*, 855.

[18] M. T. Dang, L. Hirsch, G. Wantz, *Adv. Mater.* **2011**, *23*, 3597.

[19] X. Guo, C. Cui, M. Zhang, L. Huo, Y. Huang, J. Hou, Y. Li, *Energy Environ. Sci.* **2012**, *5*, 7943.

[20] S. Holliday, R. S. Ashraf, A. Wadsworth, D. Baran, S. A. Yousaf, C. B. Nielsen, C.-H. Tan, S. D. Dimitrov, Z. Shang, N. Gasparini, M. Alamoudi, F. Laquai, C. J. Brabec, A. Salleo, J. R. Durrant, I. McCulloch, *Nat. Commun.* **2016**, *7*, 11585.

[21] A. Wadsworth, Z. Hamid, M. Bidwell, R. S. Ashraf, J. I. Khan, D. H. Anjum, C. Cendra, J. Yan, E. Rezasoltani, A. A. Y. Guilbert, M. Azzouzi, N. Gasparini, J. H. Bannock, D. Baran, H. Wu, J. C. de Mello, C. J. Brabec, A. Salleo, J. Nelson, F. Laquai, I. McCulloch, *Adv. Energy Mater.* **2018**, *8*, 1801001.

[22] Z. Ding, J. Kettle, M. Horie, S. W. Chang, G. C. Smith, A. I. Shames, E. A. Katz, *J. Mater. Chem. A* **2016**, *4*, 7274.
[23] N. P. Holmes, S. Ulum, P. Sista, K. B. Burke, M. G. Wilson, M. C. Stefan, X. Zhou, P. C. Dastoor, W. J. Belcher, *Solar Energy Materials and Solar Cells* **2014**, *128*, 369.
[24] F. Liu, D. Chen, C. Wang, K. Luo, W. Gu, A. L. Briseno, J. W. P. Hsu, T. P. Russell, *ACS Appl. Mater. Interfaces* **2014**, *6*, 19876.
[25] A. M. Ballantyne, L. Chen, J. Dane, T. Hammant, F. M. Braun, M. Heeney, W. Duffy, I. McCulloch, D. D. C. Bradley, J. Nelson, *Adv. Funct. Mater.* **2008**, *18*, 2373.
[26] S. F. Hoefler, T. Rath, N. Pastukhova, E. Pavlica, D. Scheunemann, S. Wilken, B. Kunert, R. Resel, M. Hobisch, S. Xiao, G. Bratina, G. Trimmel, *J. Mater. Chem. A* **2018**, *6*, 9506.
[27] K. D. Deshmukh, R. Matsidik, S. K. K. Prasad, L. A. Connal, A. C. Y. Liu, E. Gann, L. Thomsen, J. M. Hodgkiss, M. Sommer, C. R. McNeill, *Adv. Funct. Mater.* **2018**, *28*, 1707185.
[28] M. A. Alamoudi, J. I. Khan, Y. Firdaus, K. Wang, D. Andrienko, P. M. Beaujuge, F. Laquai, *ACS Energy Lett.* **2018**, *3*, 802.
[29] R. Mauer, M. Kastler, F. Laquai, *Adv. Funct. Mater.* **2010**, *20*, 2085.
[30] G. L. Kabongo, P. S. Mbule, G. H. Mhlongo, B. M. Mothudi, K. T. Hillie, M. S. Dhlamini, *Nanoscale Res. Lett.* **2016**, *11*, 418.
[31] I. A. Howard, R. Mauer, M. Meister, F. Laquai, *J. Am. Chem. Soc.* **2010**, *132*, 14866.
[32] J. Jaumot, R. Gargallo, A. de Juan, R. Tauler, *Chemom. Intell. Lab. Syst.* **2005**, *76*, 101.
[33] S. Albrecht, W. Schindler, J. Kurpiers, J. Kniepert, J. C. Blakesley, I. Dumsch, S. Allard, K. Fostiropoulos, U. Scherf, D. Neher, *J.Phys. Chem. Lett.* **2012**, *3*, 640.
[34] J. Kniepert, I. Lange, N. J. van der Kaap, L. J. A. Koster, D. Neher, *Adv. Energy Mater.* **2014**, *4*, 1301401.
[35] S. Karuthedath, A. Melianas, Z. Kan, V. Pranculis, M. Wohlfahrt, J. I. Khan, J. Gorenflot, Y. Xia, O. Inganäs, V. Gulbinas, M. Kemerink, F. Laquai, *J. Mater. Chem. A* **2018**, *6*, 7428.
[36] J. Kniepert, M. Schubert, J. C. Blakesley, D. Neher, *J.Phys. Chem. Lett.* **2011**, *2*, 700.
[37] U. Würfel, M. Unmüssig, *Solar RRL* **2018**, *2*, 1800229.

Higher is not necessarily better. The power conversion efficiency of P3HT:O-IDTBR bulk heterojunction solar cells peaks at intermediate (34kDa) polymer molecular weights (MWs). Combined transient absorption and time-delayed collection field experiments demonstrate that charges are generated more efficiently at intermediate P3HT MWs compared to high and low MWs.

Keyword: Non-fullerene acceptors

Jafar I. Khan[†1], Raja S. Ashraf[†1,2], Maha A. Alamoudi[1], Mohammed N. Nabi[1], Hamza N. Mohammed[3], Andrew Wadsworth[4], Yuliar Firdaus[1], Weimin Zhang[1], Thomas D. Anthopoulos[1], Iain McCulloch[1], Frédéric Laquai[1]**

P3HT Molecular Weight Determines the Performance of P3HT:O-IDTBR Solar Cells

ToC figure